Compensated Ferrimagnetism in the Zero-Moment Heusler Alloy Mn_{3}Al

Michelle E. Jamer, Yung Jui Wang, Gregory M. Stephen, Ian J. McDonald, Alexander J. Grutter, George E. Sterbinsky, Dario A. Arena, Julie A. Borchers, Brian J. Kirby, Laura H. Lewis, Bernardo Barbiellini, Arun Bansil, and Don Heiman

Phys. Rev. Applied **7**, 064036 — Published 30 June 2017

DOI: 10.1103/PhysRevApplied.7.064036

Realization of zero moment ferrimagnetic Heusler Mn_3Al

Michelle E. Jamer,[1,2] Yung Jui Wang,[2] Gregory M. Stephen,[2] Ian J. McDonald,[3,4] Alexander J. Grutter,[1] George E. Sterbinsky,[5] Dario A. Arena,[6] Julie A. Borchers,[1] Brian J. Kirby,[1] Laura H. Lewis,[3,4] Bernardo Barbiellini,[2] Arun Bansil,[2] and Don Heiman[2]

[1] *NIST Center for Neutron Research, National Institute of Standards and Technology, Gaithersburg, MD 20899, USA*
[2] *Department of Physics, Northeastern University, Boston, MA 02115 USA*
[3] *Department of Chemical Engineering, Northeastern University, Boston, MA 02115 USA*
[4] *Department of Mechanical and Industrial Engineering, Northeastern University, Boston, MA 02115 USA*
[5] *Advanced Photon Source, Argonne National Laboratory, Argonne, IL 60439, USA*
[6] *Deparment of Physics, University of South Florida, Tampa, FL 33620*

(Dated: May 19, 2017)

While antiferromagnets have been proposed as components to limit stray magnetic fields, their inability to be spin polarized inhibits their use in spintronic devices. Compensated ferrimagnets are a unique solution to this dilemma since they have zero net moment, but their nonsymmetric density of states allows achievement of full spin polarization. Density functional theory predicts Mn_3Al in the $D0_3$ structure to be fully compensated and retain half-metallicity at room temperature. In this work, 50 nm Mn_3Al thin films were synthesized using molecular beam epitaxy and annealed at various temperatures in order to investigate their magnetic properties. Magnetometry measurements confirmed the high Curie temperature of 605 K. Polarized neutron reflectometry (PNR) indicated a low net magnetic moment, along with depth profiles of the structure and magnetization. From the PNR data, we extract a saturation moment of 0.11 ± 0.04 μ_B/f.u., confirming the nominal zero moment present in these thin films.

I. Introduction

For future spintronic devices, it will be advantageous to limit extraneous magnetic interactions, which can negatively impact the spin polarization of electrons. While antiferromagnets have been proposed as components in various spintronic devices to eliminate these stray fields, the antiferromagnetic band structure prohibits spin polarization of the bulk carriers.[1] Compensated ferrimagnets provide a unique solution to this problem, with a net zero moment and a band structure which allows for spin-polarized carriers.[2–4] Recently, several Heusler materials have been suggested as spin-polarized compensated ferrimagnets.[5–7] Here we investigate nominally zero-moment Mn_3Al thin films, which were synthesized using molecular beam epitaxy (MBE) on GaAs substrates.

It is interesting to compare the magnetic properties of V_3Al and Mn_3Al, which share the same $D0_3$ crystal structure. Mn_3Al exhibits ferrimagnetism, while V_3Al is antiferromagnetic. Moreover, the asymmetric electronic properties of Mn_3Al allow the system to become half-metallic, but spin polarization is prohibited by the symmetric electronic structure of V_3Al. The G-type antiferromagnetic structure of V_3Al is shown in Fig. 1 (lower left).[8, 9] The $D0_3$ Mn_3Al structure is based on the full Heusler space group $Fm\bar{3}m$, which has the formula X_2YZ where X and Y are equal, leading to the formula X_3Z. Figure 1 (lower right) illustrates two distinguishable Mn positions in Mn_3Al: Mn(X) atoms at the Wyckoff $4b$ $(\frac{1}{2},\frac{1}{2},\frac{1}{2})$ positions and Mn(Y) atoms at the $8c$ $(\frac{1}{4},\frac{1}{4},\frac{1}{4})$ positions. Note that there are half as many Mn(Y) atoms as the Mn(X) atoms and that they occupy the octahedral sites surrounded by eight Mn(X) atoms. The Z atom occupies the $4a$ (0,0,0) position labeled as Al(Z).[10] Recently, $D0_3$-type V_3Al was synthesized and determined to behave as a gapless semiconductor, where both the majority (red) and minority (blue) bands in the DOS are symmetric, prohibiting spin polarization as depicted in Fig. 1 (upper left)[11, 12]. In the case of Mn_3Al, Mn moments are predicted to order into a compensated ferrimagnet[4, 13], shown in Fig. 1 (right lower), which allows the DOS to behave as a half-metal as seen in Fig. 1 (upper right).[14–16]

Compensated ferrimagnets are ideal for room-temperature, high-density magnetic memory applications. Mn_3Al is especially promising for giant tunable, exchange-bias applications, since Mn has a strong localized magnetic moment.[17] Developing Mn_3Al for exchange-bias applications could allow for an extremely large exchange bias at room temperature in spin-valve sensors without the use of rare earth magnets, as previously shown in Mn-Ga systems.[17] In addition, the low net magnetization, which prevents the demagnetization of surrounding components and limits stray field interactions, is expected to lead to suppressed damping and high switching speeds. These superior properties would be advantageous for terahertz spin-torque oscillators.[18]

II. Electronic structure of Mn_3Al

First-principles calculations of the band structure of Mn_3Al were performed within the framework of the density functional theory (DFT) by using projected augmented wave pseudopotentials[19] as implemented in the VASP package.[20] Generalized gradient approximation

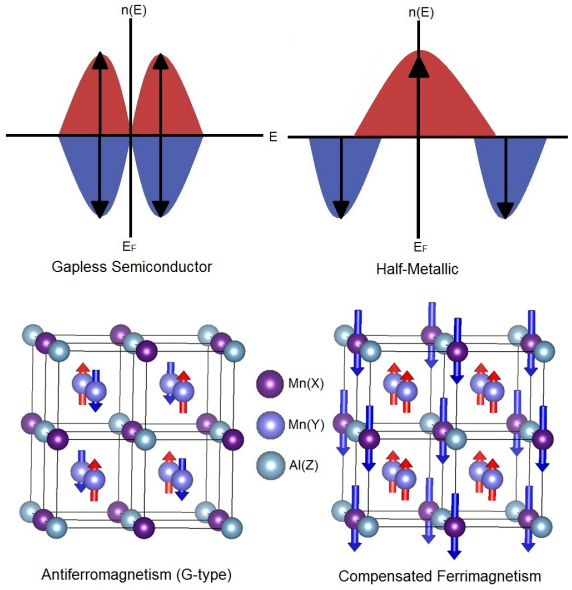

FIG. 1. Schematic density of states and magnetic structure of $D0_3$ compounds. (left upper) Density of states of a gapless semiconductor showing the majority and minority bands. (left lower) G-type antiferromagnetic structure of V_3Al. (right upper) Density of states schematic of half-metallic materials. (right lower) Proposed magnetic lattice of Mn_3Al which is a compensiated ferrimagnet.

(GGA)[21] was used for treating exchange-correlation effects. The GGA plays a crucial role in stabilizing magnetic structures compared to the local-spin-density approximation (LSDA)[22]. The Brillouin zone is integrated by using a $16 \times 16 \times 16$ k-point mesh with 360 eV cutoff energy.

For the cubic $Fm\bar{3}m$ $D0_3$ phase, the lattice parameter of $a = 5.79$ Å was determined by minimizing the total energy using the fitting method of the Murnaghan's equation of state[23, 24]. The corresponding magnetic structure was found to be a compensated ferrimagnet as shown in Fig.1 (lower right) in which the Mn(X), Mn(Y) and Al atomic sites carry magnetic moments of -2.79, 1.40, and -0.02 μ_B, respectively, and the net magnetic moment summed over all atomic sites is nearly fully compensated. The computed lattice constant and magnetic structure are consistent with previous calculations.[7]

Figure 2 shows the computed spin-polarized partial density of states (PDOS) per atom projected on the distinct atomic sites of Mn_3Al. The Fermi energy is set at 0 eV. Figures 2(a)-(d) show Mn(X)-d, Mn(Y)-d and Al-p PDOS of the cubic phase with lattice constant a = 5.79 Å. The magnetic moments mostly develop on Mn(X) and Mn(Y) sites. The asymmetric shape of the spin-resolved PDOS indicates that the Mn(X) sites host spin-down majority states, while the Mn(Y) sites host spin-up majority states. Compared to the highly spin-polarized effects on Mn(X) and Mn(Y) sites, the PDOS on the Al atoms exhibit much less spin-polarization. It is interesting to note that the PDOS at Mn(X), Mn(Y) and Al sites between -0.2 and 0.2 eV near the Fermi energy are mostly composed of spin-down states, leading to a very high degree of spin-polarization. Accordingly, our magnetic structure calculations confirm the half-metallicity and overall compensated magnetic moment in cubic phase Mn_3Al.[4, 7, 13, 14]

Recently, tetragonally distorted thin films of related Heusler compounds have been grown epitaxially on GaAs(100), with an in-plane lattice constant $a = 5.65$ Å[25, 26]. In our DFT calculations of Mn_3Al with tetragonal distortion, the c-lattice parameter was taken to be 5.90 Å. Despite the tetragonal distortion, our calculations reveal only a small change in magnetic moments with -2.61μ_B, 1.31 μ_B and -0.02 μ_B on Mn(X), Mn(Y) and Al atomic sites respectively. In addition, the Mn(X)-d, Mn(Y)-d and Al-p PDOS of the tetragonal phase shown in Fig. 2 (e)-(h) are very similar to the corresponding PDOS of the cubic phase. Therefore, the magnetic moments and PDOS results show half-metallic properties and almost fully compensated ferrimagnetic structures in both cubic and tetragonal phases of Mn_3Al. These magnetic properties appear to be therefore robust against small lattice distortions.

III. Experimental Details

Mn_3Al thin films (50 nm nominal thickness) were grown on desorbed GaAs (001) substrates using an ultra-high vacuum MBE apparatus employing separate thermal evaporation sources. The GaAs substrates underwent surface oxide removal via heating the substrate to 650 ^{o}C for 15 minutes in $\approx 10^{-3}$ Pa As flux.[25] Reflection high energy electron diffraction (RHEED) patterns indicated successful removal of the surface oxide. The Mn_3Al films were deposited epitaxially at 200 ^{o}C on the desorbed GaAs substrates. During the deposition, the RHEED pattern was collected to monitor the crystallographic ordering and alignment of the surface atoms. The thin films were further annealed after deposition at 300 ^{o}C, 325 ^{o}C, 350 ^{o}C and 400 ^{o}C for 30 minutes in ultra-high vaccuum ($\approx 10^{-7}$ Pa) to investigate the effects of annealing on the structure. Scanning electron microscopy and energy dispersive spectroscopy confirmed the composition to be within 2% variation of intended stoichiometry across the thin films. X-ray diffraction (XRD) measurements of the thin films were performed using Cu-Kα source with average wavelength $\lambda = 1.5418$ Å. In addition, X-ray absorption spectroscopy was used to measure the valence states of the Mn d-orbitals at beamline U4B at the National Synchrotron Light Source (NSLS). Magnetic characterization was performed using a superconducting quantum interference device (SQUID) magnetometer with a maximum applied field of 5 T in the temperature range 5-400 K. For higher temperature measurements (300-800 K), a vibrating sample magnetometer (VSM) was utilized. Resistivity measurements were carried out using a conductivity probe modified for

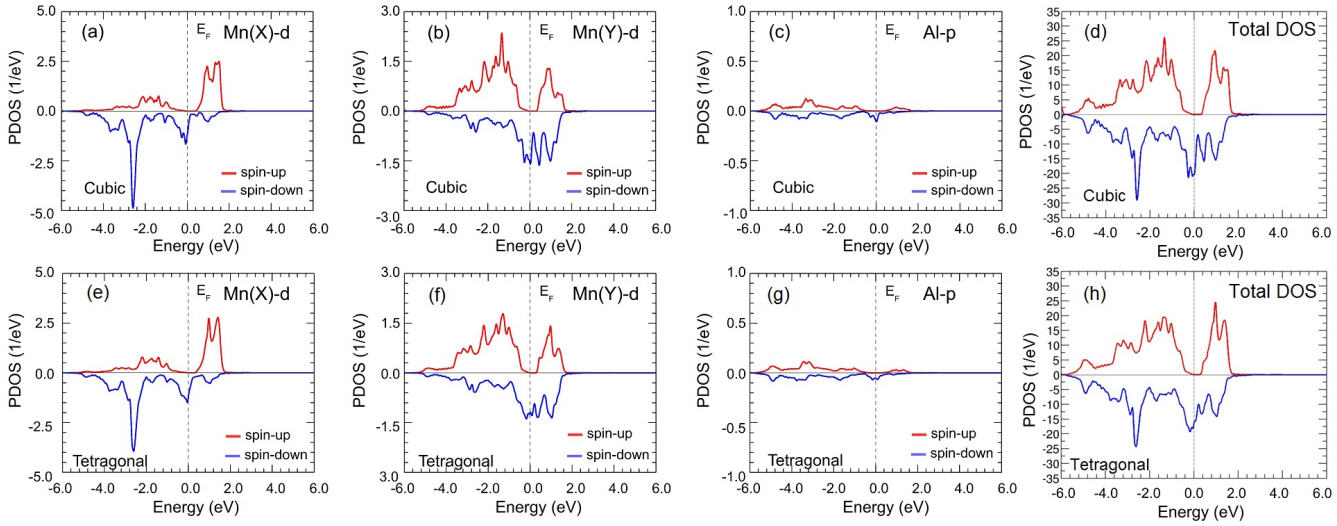

FIG. 2. Spin-polarized PDOS per atom on the distinct atomic sites of Mn_3Al. Fermi energy is set at 0 eV. (a)-(d) Mn(X)-d, Mn(Y)-d, and Al-p PDOS of the cubic phase with lattice constant $a = 5.79$ Å; while Fig. 2(e)-(h) show Mn(X)-d, Mn(Y)-d and Al-p PDOS of the tetragonal phase with lattice constants $a = 5.65$ Åand $c = 5.90$ Å. The value of $a = 5.65$ Å is chosen to be equal to that of the GaAs substrate.

use in the SQUID magnetometer.[28] The net in-plane magnetization of the thin films as a function of depth was deduced from the polarized neutron reflectometry (PNR) experiments, carried out using the PBR beamline at the NIST Center for Neutron Research. The incident and scattered neutrons were spin-polarized (>97 % efficiency) to enable determination of the parallel and perpendicular magnetization components with respect to applied field (700 mT at 100 K). The non-spin flip components, R^{++} and R^{--} (where +/- refer to the neutron moment parallel or antiparallel to the applied field, respectively) can be used to determine the scattering length density depth profile which has nuclear (ρ_N) and magnetic (ρ_M, proportional to the projection of the sample magnetization parallel to the applied field) contributions. Refl1D analysis software was used to refine the PNR model and fit the data.[29, 30]

IV. Experimental Results

The growth-axis X-ray diffraction patterns of the Mn_3Al samples are shown in Fig. 3(a) as a function of annealing temperature. The RHEED pattern shown in the inset of Fig. 3(a) indicates polycrystalline growth in the as-grown sample.[25] The lattice constant for the as-grown state at 200^{o}C (a200) was found to be $a = 5.79 \pm 0.09$ Å, in excellent agreement with the predicted lattice constant in this work. As the annealing temperature was increased to 300^{o}C (a300), three sharp Bragg peaks emerge, as indicated by the diamond data markers, which may be attributed to mixing of the GaAs and Mn_3Al in the interfacial region. However, the (311) Bragg peak remained in the pattern and the lattice constant was decreased to 5.68 ± 0.05 Å. The $D0_3$ lattice further deteriorated after the films were annealed to 325 °C (a325), indicated by the appearance of additional Bragg peaks in the XRD pattern. In the a325 pattern, more peaks emerge which can be indexed to α-Mn and Al, indicating that the lattice became more phase segregated.

X-ray absorption spectroscopy (XAS) aided in the structural analysis by providing information concerning changes in Mn d-orbital occupancy at the L_3 and L_2 edges seen in Fig. 3(b).[31–34] Comparison with reference spectrum[27] reveals that the a200 sample has a pure valence state of Mn^{2+}. However, there is a change in valence states after annealing. It is seen that after annealing to 300^o C and higher, the relative Mn^{3+} contribution increases. The XAS, however, only probes the Mn surface layer and may not be indicative of the film as a whole.[35] Since there is an AlO_x capping layer to prevent thin-film oxidation, the change in the oxidation state suggested by the XAS data could be driven by oxygen infiltration into the Mn_3Al film during annealing, or it may reflect the additional interfacial oxygen at the Mn_3Al/AlO_x boundary. Mn absorption edges are further discussed in the Supplemental material.[36]

Transport properties were measured as a function of temperature over 5-300 K. Figure 4(a) shows the zero-field resistivity ρ_{xx}(T), which indicates semiconducting behavior. At low temperature, the resistivity is consistent with an intrinsic semiconductor in that the ρ_{xx}(T) fits to the linear form $\rho_{xx} = \rho_0[1+\gamma(T-T_0)]$, where γ is the temperature coefficient of resistivity and T_0 is the reference temperature of 100 K. It is important to note that this model is only valid around the reference temperature, where γ was found to be -7.4×10^{-4} K^{-1}. However, at temperatures greater than 100 K, resistivity

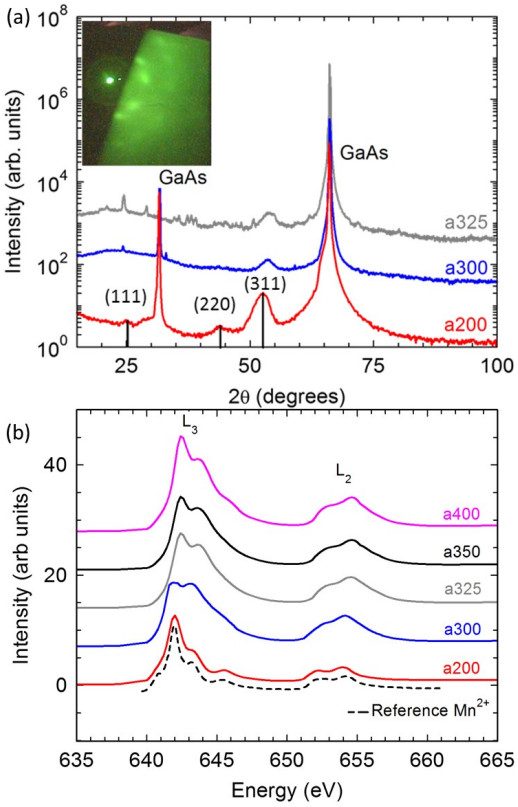

FIG. 3. (a) XRD of Mn_3Al as a function of annealing temperature, indicating that the thin film is textured in the [311] direction. (inset) The RHEED pattern indicates that the Mn_3Al grew on GaAs in a semi-polycrystalline ordering as indicated by the ring of spots. (b) The X-ray absorption spectroscopy curves for the Mn $L_{3,2}$ edges as a function of annealing temperature. The a200 sample is in the Mn^{2+} valence state as confirmed by the reference spectrum from Qiao et al[27], however there is a mixture of Mn^{2+} and Mn^{3+} states after the sample is annealed.

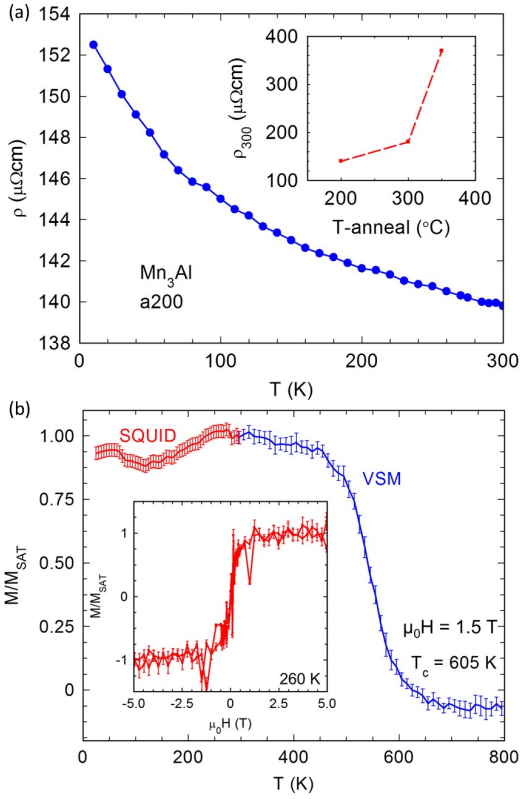

FIG. 4. (a) Electrical resistivity ρ_{xx}(T) of the a200 sample. Inset shows the ρ_{300} of the samples as a function of annealing temperature, indicating that the resistivity increases as the samples are annealed at increasing temperatures likely due to phase segregation. (b) Zero-field cooled magnetometry data of the as-grown (a200) Mn_3Al thin film. The magnetization of the film saturates quickly as a function of increasing field (inset) and the Curie temperature is approximately 605 K.

can be modeled as a sum of metallic and semiconducting contributions[25]

$$\frac{1}{\rho_{xx}} = \sigma_{xx}(T) = n_m e\mu_m(T) + n_s e\mu_s(T), \qquad (1)$$

where m and s refer to the metallic and semiconducting components, respectively. The metallic carrier concentration n_m is taken to be a constant. The inverse mobilities are additive, as they represent series resistances, and are given by $\mu_i^{-1} = (\alpha_i T + \beta_i)^{-1}$, where each conducting channel (metallic or semiconducting) i will have different values for α and β. The α term results from electron-phonon scattering while β corresponds to the mobility due to defects at T = 0 K. The fit assumes that the number of thermally activated carriers varies as $n_s(T) = e^{-\Delta E/k_B T}$ with activation energy ΔE.[25, 37, 38] Fitting to this model [red solid curve in Fig. 3(a)] gives temperature coefficients α_m and α_s close to zero, suggesting that the mobility of Mn_3Al is heavily dominated by defect scattering rather than phonons. An activation energy of $\Delta E = 14 \pm 2$ meV was found. The room-temperature resistivity (ρ_{300}) as a function of the annealing temperature was measured for a200, a300, and a350 samples and is shown in the inset in Fig. 4(a). The as-grown (a200) ρ_{300} value is 140 $\mu\Omega$cm, which is close to values for Mn_2CoAl[25] and Cr_2CoGa[26]. The resistivity slightly increases after annealing for the a300 sample to 170 $\mu\Omega$cm, but there is a dramatic increase to $\approx$ 370 $\mu\Omega$cm after annealing in the a350 sample. This rapid increase in ρ_{300} is consistent with the system becoming more disordered via phase segregation.

Magnetic moment was measured as a function of both field and temperature, with the magnetometry data displayed in Fig. 4(b). The increasing moment with increasing field for the as-grown (a200) sample (inset) is characteristic of a ferrimagnet that is not totally compensated at 260 K. The temperature dependence of the saturation magnetization (μ_0H = 1.5 T) indicates that the as-grown sample has a Curie temperature (T_C) of 605 K. The small change in magnetization of the film below 200 K could possibly arise from subtle changes in the film's magnetocrystalline anisotropy at low temperatures.

The magnetic moment measured using the SQUID as well as VSM magnetometers had a large diamagnetic contribution from the substrate, inhibiting accurate determination of the absolute moment per formula unit (f.u.). To remedy this, PNR was used to probe the net magnetization in the Mn_3Al layer for the a200 and a300 samples. Figure 5(a) displays the R^{++} and R^{--} reflectivities as a function of the wavevector transfer Q_z for the a200 sample at 100 K under an applied field of 0.7 T. The spin asymmetry (SA) emphasizes the magnetic contribution to scattering and is calculated by

$$SA = \frac{R^{++} - R^{--}}{R^{++} + R^{--}}, \tag{2}$$

as shown in Fig. 5(b).

Figure 5(c) shows the structural (ρ_N) and magnetic (ρ_M) scattering length profiles obtained from the best fits of the reflectometry data [solid lines in Fig. 5(a)]. In the nuclear profile there is evidence of a distinct interface layer between the GaAs and Mn_3Al layers (assumed unmagnetized in our model) caused by incomplete desorption of the substrate. Results obtained from the best fit to the data are consistent with the existence of a magnetic dead layer of thickness 8.9 ± 2.8 nm adjacent to the interface layer [Fig. 5(c)]. The magnetization calculated from the fit was 23 ± 8 emu/cm^3 (1 emu = 1 kA m^{-1}), consistent with a small magnetic moment in the relevant layer corresponding to 0.11 ± 0.04 μ_B/f.u. While the fit shown in Figs. 5(a) and 5(b) best captures the features of the measured reflectivity and spin asymmetry, there is a distribution in the fitted values for the thickness of the magnetic dead layer. The error in this value was thus estimated by exploring a series of models that describe the data reasonably well, as discussed in the Supplemental material.[36] The measured magnetization is greater than the corresponding theoretical value possibly due to the presence of paramagnetic Mn crystallites or a secondary magnetic phase in our samples. Alternative fits that support the choice of the best fit for the a200 sample and the fit used for the a300 sample are provided in the Supplemental material.[36] PNR results indicate that the Mn_3Al magnetic moment for a300 corresponds to a value 30 ± 5 emu/cm^3 (0.15 ± 0.03 μ_B/f.u.).

V. Conclusion

Compensated ferrimagnetism in $D0_3$ Mn_3Al was computationally and experimentally confirmed in this study. The first principles analysis yields a low net magnetization of 0.017 μ_B/f.u. at a lattice constant of a = 5.79 Å. X-ray diffraction measurements show the presence of strong [311] texturing of the $D0_3$ structure. Mn L-edge X-ray absorption spectroscopy reveals that the valence state is Mn^{2+} in the as-grown sample, and the valence state increases as the annealing temperature increases. Electrical transport of the material behaves as a semiconductor at low temperatures, but above 100 K, it displays a combined semiconductor-metallic form, which involves low energy states with an activation energy of 14 meV. The resistivity at room temperature increased after the sample was annealed, consistent with the notion that Mn_3Al lattice becomes phase segregated after annealing at 300 ^{o}C. Magnetization measurements determined a high T_C value of 605 K, while PNR measurements reveal a weak net magnetization of 0.11 ± 0.04 μ_B in the Mn_3Al layer. Our successful growth and stabilization of a Heusler compound with nearly zero net magnetization opens new materials opportunities for spintronics applications.

VI. Acknowledgements

We thank T. Hussey for assistance with magnetometry, D. Gilbert, B.A. Assaf and C.A. Lane for helpful discussions, and G. Player and M.C. DeCapua for general assistance. The experimental work at Northeastern University was supported by the National Science Foundation grant ECCS-1402738. The work of AB group at Northeastern University was supported by the US Department of Energy (DOE), Office of Science, Basic Energy Sciences grant number DE-FG02-07ER46352 (core research), and benefited from Northeastern University's Advanced Scientific Computation Center (ASCC), the NERSC supercomputing center through DOE grant number DE-AC02-05CH11231, and support (applications to layered materials) from the DOE EFRC: Center for the Computational Design of Functional Layered Materials (CCDM) under grant number DE-SC0012575.

[1] J.M.D. Coey. *Magnetism and Magnetic Materials*. Cambridge University Press, 1 edition (2009).

[2] H. Kurt, K. Rode, P. Stamenov, M. Venkatesan, Y.-C. Lau, E. Fonda, and J.M.D. Coey, Cubic Mn_2Ga thin films: Crossing the spin gap with ruthenium, Phys. Rev. Lett. 112, 027201 (2014).

[3] M.E. Jamer, L.G. Marshall, G.E. Sterbinsky, L.H. Lewis, and D. Heiman, Low-moment ferrimagnetic phase of the Heusler compound Cr_2CoAl, J. Magn. Magn. Mater. 394, 32-36 (2015).

[4] S. Wurmehl, H.C. Kandpal, G. Fecher, and C. Felser, Valence electron rules for prediction of half-metallic compensated-ferrimagnetic behaviour of Heusler compounds with complete spin polarization, J. Phys.: Condens. Matter 18, 6171–6181 (2006).

[5] X.L. Wang, Proposal for a New Class of Materials: Spin Gapless Semiconductors, Phys. Rev. Lett. 100, 156404 (2008).

[6] H. Hakimi, M. Venkatesan, K. Rode, K. Ackland, and J.M.D. Coey, The zero-magnetization Heusler ferrimagnet, J. Appl. Phys. 113, 17B101, (2013).

[7] G.Y. Gao and K.L. Yao, Antiferromagnetic half-metals, gapless half-metals, and spin gapless semiconductors: The $D0_3$-type Heusler alloys, Appl. Phys. Lett. 103, 232409 (2013).

[8] M.E. Jamer, B.A. Assaf, G.E. Sterbinsky, D.A. Arena, L.H. Lewis, A.A. Saúl, G. Radtke, and D. Heiman, Antiferromagnetic phase of the gapless semiconductor V_3Al, Phys. Rev. B 91, 094409 (2015).

[9] I. Galanakis, S. Tirpanci, K. Özdoğan, and E. Sasiğlu, Itinerant G-type antiferromagnetism $D0_3$-type V_3Z (Z=Al, Ga,In) compounds: A first-principles study, Phys. Rev. B 94, 06440 (2016).

[10] A. Bansil, S. Kaprzyk, P.E. Mijnarends, and J. Toboła, Electronic structure and magnetism of $Fe_{3-x}V_xX$ (X=Si, Ga, and Al) alloys by the KKR-CPA method, Phys. Rev. B 60, 13396 (1999).

[11] X.T. Wang, Z.X. Cheng, J.L. Wang, X.L. Wang, and G.D. Liu, A full spectrum of spintronic properties demonstrated by a $C1_b$-type Heusler compound Mn_2Sn subjected to strain engineering, J. Mater. Chem. C, 4, 8535 (2016).

[12] X. L. Wang, S. X. Dou, and C. Zhang, Zero-gap materials for future spintronics, electronics and optics, NPG Asia Mater. 2, 31-38 (2010).

[13] H. Luo, Z. Zhu, L. Ma, S. Xu, Z. Zhu, C. Jiang, H. Xu, and G. Wu, Effect of site preference of 3d atoms on the electronic structure and half-metallicity of Heusler alloy Mn_2YAl, J. Phys. D: Appl. Phys. 41, 055010 (2008).

[14] S.M. Azar, B.A. Hamad, and J.M. Khalifeh, Structural, electronic and magnetic properties of $Fe_{3-x}Mn_xZ$ (Z=Al, Ge,Sb) Heusler alloys, J. Magn. Magn. Mater. 324, 1776-1785 (2012).

[15] S. Skaftouros, K. Özdoğan, E. Sasiğlu, and I. Galanakis, Search for spin gapless semiconductors: The case of inverse Heusler compounds, Appl. Phys. Lett. 102, 022402 (2013).

[16] S. Skaftouros, K. Özdoğan, E. Sasiğlu, and I. Galanakis, Generalized Slater-Pauling rule for the inverse Heusler compounds, Phys. Rev. B 87, 022420 (2013).

[17] A.K. Nayak, M. Nicklas, S. Chadov, P. Khuntia, C. Shekhar, A. Kalache, M. Baenitz, Y. Skourski, V.K. Guduru, A. Puri, U. Zeitler, J.M.D. Coey, and C. Felser, Design of compensated ferrimagnetic Heusler alloys for giant tunable exchange bias, Nature Mater. 14, 679-684, (2015).

[18] D. Betto, K. Rode, N. Thiyagarajah, Y.C. Lau, K. Borisov, G. Atcheson, M. Zic, T. Archer, P. Stamenov, and J.M.D. Coey, The zero-moment half metal: How could it change spin electronics, AIP Advances 6, 055601 (2016).

[19] G. Kresse and D. Joubert. From ultrasoft pseudopotentials to the projector augmented-wave method, Phys. Rev. B 59, 1758 (1999).

[20] J.P. Perdew, K. Burke, and M. Ernzerhof, Generalized Gradient Approximation Made Simple, Phys. Rev. Lett. 77, 3865 (1996).

[21] G. Kresse and J. Hafner, *Ab initio molecular dynamics for open-shell transition metals*, Phys. Rev. B 48, 13115 (1993).

[22] B. Barbiellini, E.G. Moroni, and T. Jarlborg, Effects of gradient corrections on electronic structure in metals, J. Phys. Condens. Matter 2, 7597 (1990).

[23] C.L. Fu and K.M. Ho, First-principles calculation of the equilibrium ground-state properties of transition metals: Applications to Nb and Mo, Phys. Rev. B 28, 5480 (1983).

[24] F.D. Murnaghan, The Compressibility of Media under Extreme Pressures, Proc. Natl. Acad. Sci. U. S. A. 30, 244–247 (1944).

[25] M.E. Jamer, B.A. Assaf, T. Devakul, and D. Heiman, Magnetic and transport properties of Mn_2CoAl oriented films, Appl. Phys. Lett. 103, 142403 (2013).

[26] M.E. Jamer, G.E. Sterbinsky, G.M. Stephen, M.C. DeCapua, G. Player, and D. Heiman, Magnetic properties of low-moment ferrimagnetic Heusler Cr_2CoGa thin films grown by molecular beam epitaxy, Appl. Phys. Lett. 109, 182402 (2016).

[27] R. Qiao, T. Chin, S.J. Harris, S. Yan, and W. Yang, Spectroscopic fingerprints of valence and spin states in manganese oxides and fluorides, Curr. Appl. Phys. 13, 544–548 (2013).

[28] B.A. Assaf, T. Cardinal, P. Wei, F. Katmis, J.S. Moodera, and D. Heiman, Modified electrical transport probe design for standard magnetometer, Rev. Sci. Instrum. 83, 033904 (2012).

[29] B. J. Kirby, P. A. Kienzle, B. B. Maranville, N. F. Berk, K.J. Krycka, F. Heinrich, and C. F. Majkrzak, Phase-sensitive specular neutron reflectometry for imaging the nanometer scale composition depth profile of thin-film materials, Curr. Opin. Colloid Interface Sci. 17, 44 (2012).

[30] NCNR. MS Windows NT kernel description, 2016. URL `https://www.ncnr.nist.gov/instruments/ng1refl/`.

[31] B.T. Thole, P. Carra, F. Sette, and G. van der Laan, X-ray circular dichroism as a probe of orbital magnetization, Phys. Rev. Lett. 68, 1943 (1992).

[32] G. van der Laan and I.W. Kirkman, The 2p absorption spectra of 3d transition metal compounds in tetrahedral and octahedral symmetry, J. Phys. Cond. Mat. 4, 4189, (1992).

[33] P. Carra, B.T. Thole, M. Altarelli, and X. Wang, X-ray circular dichroism and local magnetic fields. Phys. Rev. Lett. 70, 694 (1993).

[34] H.K Schmid and W. Mader, Oxidation states of Mn and Fe in various compound oxide systems, Micron 37, 426–432 (2006).

[35] B. Ravel and M.Newville, ATHENA, ARTEMIS, HEPHAESTUS: data analysis for X-ray absorption spectroscopy using IFEFFIT, J. Synchrotron. Radiat. 12, 537-541 (2005).

[36] M.E. Jamer, Y.J. Wang, G.M. Stephen, I.J. McDonald, A.J. Grutter, G.E. Sterbinsky, D.A. Arena, J. Borchers, B.J. Kirby, L.H.Lewis, B. Barbiellini, A. Bansil, and D. Heiman, See Supplemental Material at [] for PNR and XAS details, (2017).

[37] L. Bainsla, A.I. Mallick, M.M. Raja, A.A. Coelho, A.K. Nigam, D.D. Johnson, A. Alam, and K.G. Suresh, Ori-

gin of spin gapless semiconductor behavior in CoFeCrGa: Theory and Experiment, Phys. Rev. B 92, 045201, (2015).

[38] L. Bainsla, A.I. Mallick, A.A. Coelho, A.K. Nigam, B.S.D. Varaprasad, Y.K. Takahashi, A. Alam, K.G. Suresh, and K. Hono, High spin polarization and spin splitting in equiatomic quaternary CoFeCrAl Heusler alloy, J. Magn. Magn. Mater. 394, 82-86 (2015).

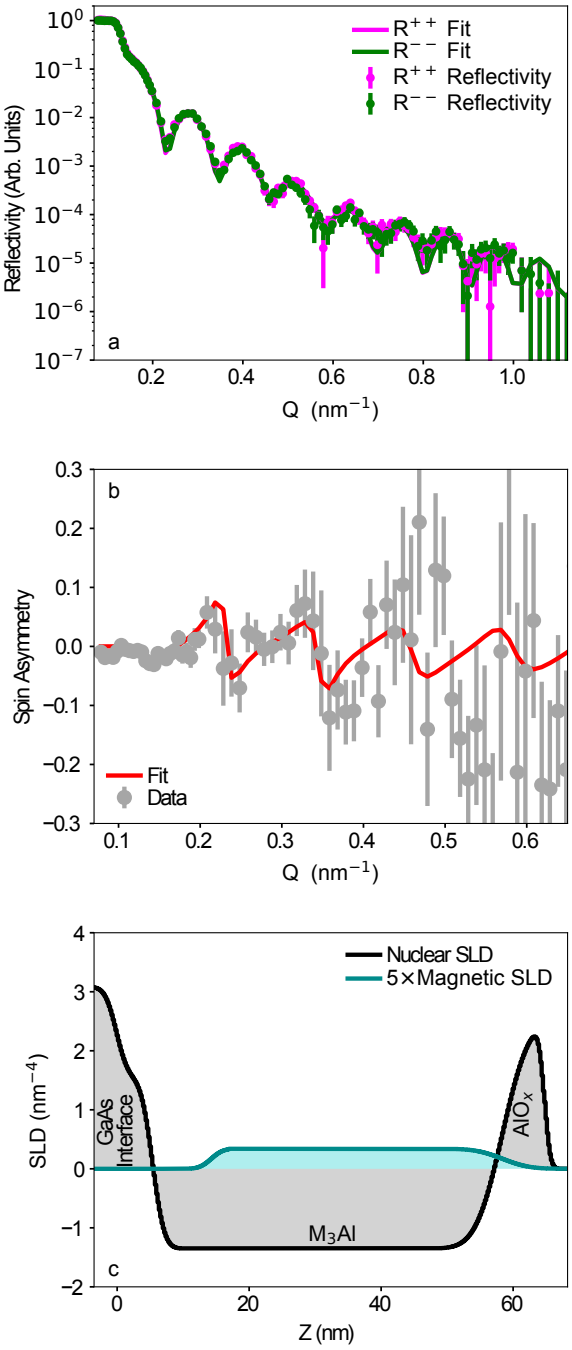

FIG. 5. (a) R^{++} and R^{--} reflectivities from the a200 sample as a function of Q_z. (b) Spin asymmetry of the reflectometry data, which tracks the magnetization within the Mn_3Al layer parallel to the applied field. (b) Profiles of the nuclear (ρ_N) and magnetic (ρ_M) scattering length density (SLD) as a function of depth (z).